Research Article | Vol. 24, No. 26 | 26 Dec 2016 | OPTICS EXPRESS 29512

Optics EXPRESS

Sub-picosecond snapshots of fast electrons from high intensity laser-matter interactions

R. Pompili,[1,*] M.P. Anania,[1] F. Bisesto,[1] M. Botton,[2] M. Castellano,[1] E. Chiadroni,[1] A. Cianchi,[3] A. Curcio,[1] M. Ferrario,[1] M. Galletti,[1] Z. Henis,[2] M. Petrarca,[4] E. Schleifer,[2] and A. Zigler[2]

[1] *Laboratori Nazionali di Frascati, 00044 Frascati, Italy*
[2] *Racah Institute of Physics, Hebrew University, 91904 Jerusalem, Israel*
[3] *University of Rome Tor Vergata, 00133 Rome, Italy*
[4] *University of Rome Sapienza, 00185 Rome, Italy*
[*] *riccardo.pompili@lnf.infn.it*

Abstract: The interaction of a high-intensity short-pulse laser with thin solid targets produces electron jets that escape the target and positively charge it, leading to the formation of the electrostatic potential that in turn governs the ion acceleration. The typical timescale of such phenomena is on the sub-picosecond level. Here we show, for the first time, temporally-resolved measurements of the first released electrons that escaped from the target, so-called fast electrons. Their total charge, energy and temporal profile are provided by means of a diagnostics based on Electro-Optical Sampling with temporal resolution below 100 fs.

© 2016 Optical Society of America

OCIS codes: (320.7090) Ultrafast lasers; (190.7110) Ultrafast nonlinear optics; (320.2250) Femtosecond phenomena; (320.7100) Ultrafast measurements; (320.7120) Ultrafast phenomena; (320.7130) Ultrafast processes in condensed matter, including semiconductors.

References and links

1. B. A. Remington, D. Arnett, R. Paul, and H. Takabe, "Modeling astrophysical phenomena in the laboratory with intense lasers," Science **284**, 1488–1493 (1999).
2. T. Bartal, M. E. Foord, C. Bellei, M. H. Key, K. A. Flippo, S. A. Gaillard, D. T. Offermann, P. K. Patel, L. C. Jarrott, and D. P. Higginson, "Focusing of short-pulse high-intensity laser-accelerated proton beams," Nat. Phys. **8**, 139–142 (2012).
3. M. Roth, T. Cowan, M. Key, S. Hatchett, C. Brown, W. Fountain, J. Johnson, D. Pennington, R. Snavely, and S. Wilks, "Fast ignition by intense laser-accelerated proton beams," Phys. Rev. Lett. **86**, 436 (2001).
4. D. Kaganovich, D. Gordon, and A. Ting, "Observation of large-angle quasimonoenergetic electrons from a laser wakefield," Phys. Rev. Lett. **100**, 215002 (2008).
5. D. Gordon, R. Hubbard, J. Cooley, B. Hafizi, A. Ting, and P. Sprangle, "Quasimonoenergetic electrons from unphased injection into channel guided laser wakefield accelerators," Phys. Rev. E **71**, 026404 (2005).
6. E. Clark, K. Krushelnick, M. Zepf, F. Beg, M. Tatarakis, A. Machacek, M. Santala, I. Watts, P. Norreys, and A. Dangor, "Energetic heavy-ion and proton generation from ultraintense laser-plasma interactions with solids," Phys. Rev. Lett. **85**, 1654 (2000).
7. R. Snavely, M. Key, S. Hatchett, T. Cowan, M. Roth, T. Phillips, M. Stoyer, E. Henry, T. Sangster, and M. Singh, "Intense high-energy proton beams from petawatt-laser irradiation of solids," Phys. Rev. Lett. **85**, 2945 (2000).
8. A. Mackinnon, Y. Sentoku, P. Patel, D. Price, S. Hatchett, M. Key, C. Andersen, R. Snavely, and R. Freeman, "Enhancement of proton acceleration by hot-electron recirculation in thin foils irradiated by ultraintense laser pulses," Phys. Rev. Lett. **88**, 215006 (2002).
9. K. W. Ledingham, P. R. Bolton, N. Shikazono, and C.-M. C. Ma, "Towards laser driven hadron cancer radiotherapy: A review of progress," Appl. Sci. **4**, 402–443 (2014).
10. J.-L. Dubois, F. Lubrano-Lavaderci, D. Raffestin, J. Ribolzi, J. Gazave, A. C. La Fontaine, E. d'Humières, S. Hulin, P. Nicolaï, and A. Poyé, "Target charging in short-pulse-laser–plasma experiments," Phys. Rev. E **89**, 013102 (2014).
11. P. K. Singh, Y. Cui, G. Chatterjee, A. Adak, W. Wang, S. Ahmed, A. D. Lad, Z. Sheng, and G. R. Kumar, "Direct observation of ultrafast surface transport of laser-driven fast electrons in a solid target," Phys. Plasmas (1994-present) **20**, 110701 (2013).
12. A. Poyé, S. Hulin, M. Bailly-Grandvaux, J.-L. Dubois, J. Ribolzi, D. Raffestin, M. Bardon, F. Lubrano-Lavaderci, E. D'Humières, and J. J. Santos, "Physics of giant electromagnetic pulse generation in short-pulse laser experiments," Phys. Rev. E **91**, 043106 (2015).

#275483 http://dx.doi.org/10.1364/OE.24.029512
Journal © 2016 Received 13 Sep 2016; revised 8 Nov 2016; accepted 8 Nov 2016; published 12 Dec 2016

Optics EXPRESS

13. A. Poyé, J.-L. Dubois, F. Lubrano-Lavaderci, E. D'Humières, M. Bardon, S. Hulin, M. Bailly-Grandvaux, J. Ribolzi, D. Raffestin, and J. Santos, "Dynamic model of target charging by short laser pulse interactions," Phys. Rev. E **92**, 043107 (2015).
14. L. Robson, P. Simpson, R. J. Clarke, K. W. Ledingham, F. Lindau, O. Lundh, T. McCanny, P. Mora, D. Neely, and C.-G. Wahlström, "Scaling of proton acceleration driven by petawatt-laser–plasma interactions," Nat. Phys. **3**, 58–62 (2007).
15. A. Macchi, M. Borghesi, and M. Passoni, "Ion acceleration by superintense laser-plasma interaction," Rev. Mod. Phys. **85**, 751 (2013).
16. S. Wilks, A. Langdon, T. Cowan, M. Roth, M. Singh, S. Hatchett, M. Key, D. Pennington, A. MacKinnon, and R. Snavely, "Energetic proton generation in ultra-intense laser–solid interactions," Phys. Plasmas (1994-present) **8**, 542–549 (2001).
17. O. Jäckel, J. Polz, S. Pfotenhauer, H. Schlenvoigt, H. Schwoerer, and M. Kaluza, "All-optical measurement of the hot electron sheath driving laser ion acceleration from thin foils," New J. Phys. **12**, 103027 (2010).
18. P. Nilson, J. Davies, W. Theobald, P. Jaanimagi, C. Mileham, R. Jungquist, C. Stoeckl, I. Begishev, A. Solodov, and J. Myatt, "Time-resolved measurements of hot-electron equilibration dynamics in high-intensity laser interactions with thin-foil solid targets," Phys. Rev. Lett. **108**, 085002 (2012).
19. A. Sandhu, A. Dharmadhikari, P. Rajeev, G. R. Kumar, S. Sengupta, A. Das, and P. Kaw, "Laser-generated ultrashort multimegagauss magnetic pulses in plasmas," Phys. Rev. Lett. **89**, 225002 (2002).
20. I. Wilke, A. M. MacLeod, W. Gillespie, G. Berden, G. Knippels, and A. Van Der Meer, "Single-shot electron-beam bunch length measurements," Phys. Rev. Lett. **88**, 124801 (2002).
21. B. Steffen, V. Arsov, G. Berden, W. Gillespie, S. Jamison, A. M. MacLeod, A. Van Der Meer, P. Phillips, H. Schlarb, and B. Schmidt, "Electro-optic time profile monitors for femtosecond electron bunches at the soft x-ray free-electron laser flash," Phys. Rev. Spec. Top.-Ac. **12**, 032802 (2009).
22. R. Pompili, M. P. Anania, M. Bellaveglia, A. Biagioni, G. Castorina, E. Chiadroni, A. Cianchi, M. Croia, D. D. Giovenale, M. Ferrario, F. Filippi, A. Gallo, G. Gatti, F. Giorgianni, A. Giribono, W. Li, S. Lupi, A. Mostacci, M. Petrarca, L. Piersanti, G. D. Pirro, S. Romeo, J. Scifo, V. Shpakov, C. Vaccarezza, and F. Villa, "Femtosecond timing-jitter between photo-cathode laser and ultra-short electron bunches by means of hybrid compression," New J. Phys. **18**, 083033 (2016).
23. M. Petrarca, S. Henin, N. Berti, M. Matthews, J. Chagas, J. Kasparian, J.-P. Wolf, G. Gatti, G. Di Pirro, and M.-P. Anania, "White-light femtosecond lidar at 100 tw power level," Appl. Phys. B **114**, 319–325 (2014).
24. M. Ferrario, D. Alesini, M. Anania, A. Bacci, M. Bellaveglia, O. Bogdanov, R. Boni, M. Castellano, E. Chiadroni, and A. Cianchi, "SPARC_LAB present and future," Nucl. Instrum. Meth. B **309**, 183–188 (2013).
25. A. L. Cavalieri, D. Fritz, S. Lee, P. Bucksbaum, D. Reis, J. Rudati, D. Mills, P. Fuoss, G. Stephenson, and C. Kao, "Clocking femtosecond x rays," Phys. Rev. Lett. **94**, 114801 (2005).
26. M. Helle, D. Gordon, D. Kaganovich, and A. Ting, "Extending electro-optic detection to ultrashort electron beams," Phys. Rev. Spec. Top.-Ac. **15**, 052801 (2012).
27. J. Badziak, S. Głowacz, S. Jabłoński, P. Parys, J. Wołowski, H. Hora, J. Krása, L. Láska, and K. Rohlena, "Production of ultrahigh ion current densities at skin-layer subrelativistic laser–plasma interaction," Plasma Phys. Contr. F. **46**, B541 (2004).
28. S. Casalbuoni, H. Schlarb, B. Schmidt, B. Steffen, P. Schmuser, and A. Winter, "Numerical studies on the electro-optic sampling of relativistic electron bunches," in "Proceedings of the Particle Accelerator Conference, 2005. PAC 2005," (IEEE, 2005), pp. 3070–3072.
29. G. Gallot, J. Zhang, R. McGowan, T.-I. Jeon, and D. Grischkowsky, "Measurements of the thz absorption and dispersion of znte and their relevance to the electro-optic detection of thz radiation," Appl. Phys. Lett. **74**, 3450–3452 (1999).
30. R. Pompili, A. Cianchi, D. Alesini, M. Anania, A. Bacci, M. Bellaveglia, M. Castellano, E. Chiadroni, D. D. Giovenale, G. D. Pirro, G. Gatti, F. Giorgianni, M. Ferrario, S. Lupi, F. Massimo, A. Mostacci, A. Rossi, C. Vaccarezza, and F. Villa, "First single-shot and non-intercepting longitudinal bunch diagnostics for comb-like beam by means of electro-optic sampling," Nucl. Instrum. Meth. A **740**, 216 – 221 (2014).

1. Introduction

The interaction of high-intensity lasers with matter is able to produce flux of charged particles (electrons, protons and ions) and electromagnetic radiation over a wide range of energy [1, 2], enabling new experiments in several research areas like laser-based acceleration [3–5]. Ion acceleration from thin foils irradiated by high-intensity short-pulse lasers, in particular, has attracted high attention during the past decade since the emitted ion and proton pulses contain a large amount of particles with energies in multi-MeV range [6–8]. This provides several possibilities for a wide range of applications in nuclear and medical physics [9]. According to the established theoretical models [10], the process acts as in the following. Some electrons are

Optics EXPRESS

directly accelerated by the impinging laser and penetrate the target. The majority of them spread and dissipate energy inside of it while the *hot* component of these electrons is able to reach the target rear side and is released in vacuum [11]. Only the most energetic of these electrons can escape, leaving behind an electrostatic potential that locks the majority of them near the target [12]. Such potential, set up by the unbalanced positive charge left on target [13], generates an electric field that ionizes and accelerates surface ions [14, 15] in a process called Target Normal Sheath Acceleration [16] (TNSA). Usually a thin layer (few nm) of hydrocarbons, water, or oxides contaminates the target surfaces so that ions with the highest charge-to-mass ratio are accelerated predominantly.

So far only indirect evidences of the escaping electron component have been recorded by measuring the radiated electromagnetic pulses [17, 18] and magnetic fields [19] but a detailed and time-resolved study of the release mechanism has not been carried out yet. Here we report direct and temporally resolved measurements of fast electrons ejected from solid targets after the interaction with a short-pulse high-intensity laser. We employed a temporal diagnostics based on Electro-Optical Sampling (EOS [20]), widely used in conventional accelerators [21, 22], that provides 'snapshots' of such electrons with sub-picosecond resolution.

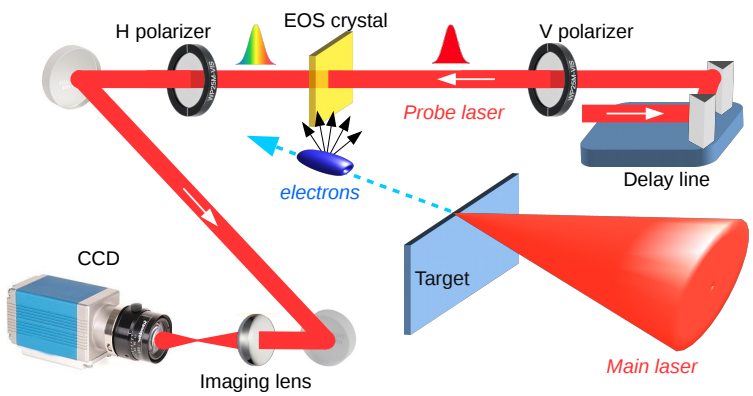

Fig. 1. Setup of the experiment. The FLAME laser is focused on a metallic target that ejects electrons. The EOS system, based on a ZnTe crystal 1 mm downstream the target, measures the temporal profile of the emitted electrons by means of an ultra-short probe laser.

2. Experimental setup

The experiment has been carried out with the FLAME laser [23] at the SPARC_LAB test-facility [24] using the setup shown in Fig. 1. It consists a 130 TW Ti:Sapphire laser system delivering 35 fs (FWHM), up to 4 J pulses at 800 nm central wavelength and 10 Hz repetition rate. The laser beam was focused $f/10$ off-axis parabolic mirror with focal length $f = 1$ m. Fast electrons are produced by irradiating the tip (about 10 μm thick) of a stainless steel wedged target with 2 J laser pulses. The $1/e^2$ diameter of the laser spot on target was approximately 60 μm. The EOS diagnostics relies on a 500 μm-thick ZnTe crystal and employs the spatial decoding technique [25], in which a probe laser enters into the crystal with an incidence angle $\theta_i \approx 28°$. A lens installed downstream the crystal is then used to image the laser on a CCD camera where the EOS signal is detected. The probe laser (35 fs pulse duration) is directly split from the FLAME laser, ensuring a jitter-free synchronization. Being $d_L \approx 6$ mm its transverse spot (fwhm), the active time window provided by the EOS is $\Delta t = (d_L/c) \cdot \sin\theta_i \approx 10$ ps, where c is the vacuum speed of light. Temporal resolutions of the order of few tens of femtoseconds have been demonstrated in past years by using different electro-optic crystals and decoding

Optics EXPRESS

techniques [26]. In our case the final resolution is less than 100 fs.

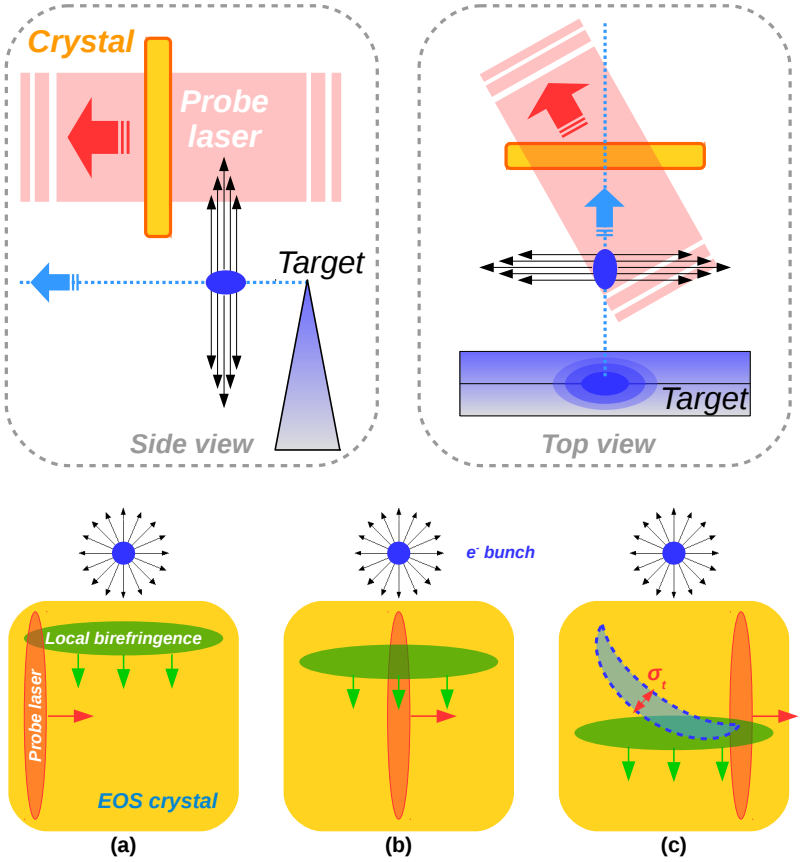

Fig. 2. (Top) Detailed view of the EOS experimental setup. The emitted bunch travels normally to the crystal surface and moves below it while the probe laser crosses the crystal with a non-zero incidence angle. (Bottom) Spatial encoding process. Due to the imaging lens employed, the signals are flipped both horizontally and vertically. (a) The bunch Coulomb fields make the crystal birefringent. (b) While the electric field penetrates in the crystal, the local birefringence shifts downwards. Simultaneously the probe laser crosses the crystal and its polarization is thus rotated. (c) The resulting signal is emitted along the blue region, i.e. where the local birefringence and the probe laser temporally overlapped.

In our setup the temporal charge profile of the emitted electron cloud is spatially imprinted along the transverse profile of the probe laser, temporally synchronized with the electrons in correspondence of the ZnTe crystal. A detailed view of the EOS setup is shown in Fig. 2(a). The ZnTe crystal is located 1 mm downstream the target. Since after the laser-solid target interaction the majority of hot electrons is confined within a distance of the order of the Debye length [27] (less than 1 μm in our experimental conditions), only the most energetic ones capable to escape the potential barrier reach the crystal and are detected during the illumination by the probe pulse. Figure 2(b) also shows the encoding process of the electron beam along the laser transverse profile. Since we used a lens in order to image the crystal on the CCD camera, the signals appear flipped both horizontally and vertically. Due to the geometry of the implemented EOS setup (electrons are moving below the crystal and normally to it while the probe laser propagates laterally from right to left), the local birefringence (induced by the electrons electric field) and

Optics EXPRESS

the probe laser temporally overlap along the dashed blue region. As a consequence the EOS signals imaged on the CCD exhibit a curved shape. The total charge and duration (indicated by σ_t in Fig. 2) of the emitted electrons is then retrieved from the signal amplitude and width, respectively.

The synchronization of the main and probe lasers in correspondence of the EOS crystal is obtained by means of an α-cut BBO crystal installed on the ZnTe holder. The time overlapping (representing our reference time) is then retrieved by looking for light emission by second-harmonic generation (SHG). For this purpose a 3 fs resolution delay-line has been installed on the probe line (see Fig. 1). Once the reference time is determined, the delay-line is moved in order to be synchronized with the emitted electrons and produce a detectable EOS signal. By measuring the relative delay with respect to the reference time it is possible to estimate the energy of the emitted electrons. Indeed, being the EOS a single-shot device, it can be used as a time of arrival monitor allowing to measure its time of flight [22, 25]. Unlike conventional time-integrated spectrometric techniques, this method is able to provide energy measurements resolved in time. Figure 3 shows the calibration of the energy as a function of the measured relative delay. It is worth noting that only the average electron energy can be estimated with such method, not the entire energy spectrum.

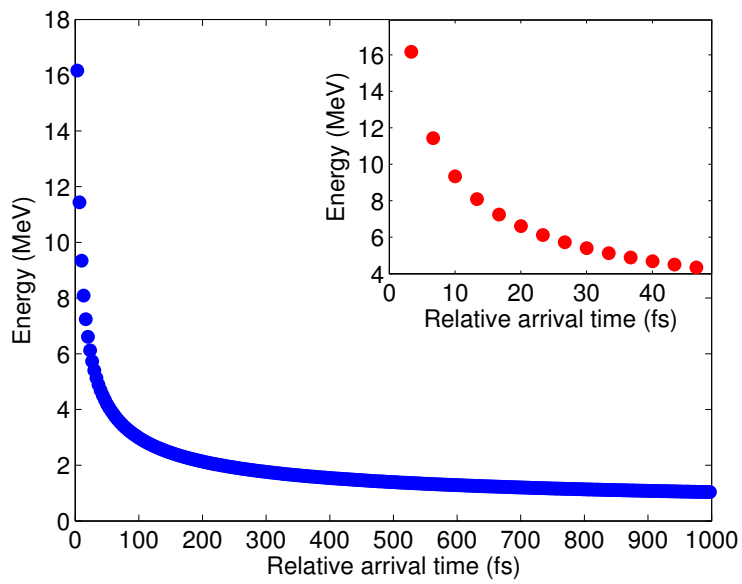

Fig. 3. Mean electron energy vs time of flight calibration. Each point corresponds to one delay line step (3 fs). The inset shows a magnification of the first part (higher energies).

3. Numerical simulations

In order to retrieve the main properties of the emitted electrons (charge, energy and duration) we developed a numerical simulation in MATLAB environment. It starts calculating the transverse electric field of an electron bunch travelling in vacuum at distance r from the ZnTe crystal,

$$E_v(r,t) = \frac{Qr}{4\pi\epsilon_0\gamma^2}\int_{-\infty}^{+\infty}\frac{\lambda(t)}{\left(z^2+r^2/\gamma^2\right)^{3/2}}dz\,, \tag{1}$$

where ϵ_0 is the vacuum permittivity, Q the bunch charge, γ the relativistic Lorentz factor and $\lambda(t)$ is the longitudinal charge density, assumed Gaussian with duration σ_t. The simulation then

Optics EXPRESS

takes into account the dispersive propagation [28] of such field in a ZnTe crystal of thickness d. Being $n(\omega)$ and $\kappa(\omega)$ the crystal refractive and absorption indices in the Fourier domain [29], the propagating field is

$$E_p(r,\omega) = A_{tr}(\omega)E_v(r,\omega)\exp\left(i\frac{\omega}{c}(n(\omega)+i\kappa(\omega))d\right), \tag{2}$$

where $A_{tr}(\omega) = 2/(n(\omega)+i\kappa(\omega)+1)$ is the amplitude transmission coefficient. ZnTe, in particular, is affected by a phonon resonance located at $\Omega_0 \approx 5.3$ THz, causing a large absorption for frequencies close to Ω_0. Consequently the field spectrum is strongly distorted for frequencies above such threshold. The sampling is then performed by a co-propagating probe laser pulse whose initial linear polarization gradually becomes elliptical due to the electro-optic effect induced by the Coulomb field. Being λ_L the laser central wavelength, the overall phase delay cumulated by the probe laser at the end of the crystal is given by the convolution

$$\Gamma(r,t) = \frac{2\pi d}{\lambda_L}n_0^3(\lambda_L)r_{41}\ E_p(r,t) * \widetilde{E}_L(t), \tag{3}$$

where n_0 and r_{41} are the ZnTe optical refractive index calculated in λ_L and its electro-optic coefficient, respectively. $\widetilde{E}_L(t)$ represents the normalized (dimensionless) laser electric field, again assumed to be Gaussian. The process terminates by simulating the signal output ($\propto \sin^2(\Gamma/2)$) on the CCD camera [30]. Since the shape and strength of the detected signals depends on the bunch parameters, we extrapolated such information by a direct comparison between the experimental data and the simulated one.

3.1. Determination of the main bunch parameters from the electro-optic signals

According to Eq. (3), the main parameters of the electrons ejected from target can be retrieved from the resulting electro-optic signals. Indeed the signal shape is strongly altered by changing the main beam parameters. If $r \ll \gamma c\sigma_t$, where σ_t is the (rms) beam duration, the observer is in the near field region and the electric field in Eq. (1) reduces to $E_v(t) \approx 2Q\lambda(t)/(4\pi\epsilon_0 r)$. On the contrary, in the far field limit ($r \gg \gamma c\sigma_t$) the field reads $E_v \approx Q\gamma/(4\pi\epsilon_0 r^2)$, i.e. the bunch is seen as a point-like charge by the observer. Figure 4 reports six different simulated cases related to electron bunches with different initial parameters, summarized in Table 1. The dependency on the total electron charge is not analyzed since the signal amplitude scales linearly. We investigated, in particular, the dependency on the bunch energy (E_0), duration (σ_t), position with respect to the crystal (x_B, y_B, with $r = \sqrt{x_B^2 + y_B^2}$) and relative delay with respect to the probe laser.

Table 1. Bunch parameters used to produce the electro-optic signals showed in Fig. 4. Here x_B represents the horizontal offset of the bunch with respect to the crystal center while y_B is the vertical distance with respect to the crystal side. The charge is 1 nC in all cases.

Figure	$\mathbf{E_0}$ (MeV)	$\sigma_\mathbf{t}$ (ps)	$\mathbf{x_B}$ (mm)	$\mathbf{y_B}$ (mm)	$\mathbf{\Delta t_{laser}}$ (ps)
4(a)	10	1	0	1	0
4(b)	1	1	0	1	0
4(c)	10	10	0	1	0
4(d)	10	1	0	10	0
4(e)	10	1	3	1	0
4(f)	10	1	0	1	4

Figure 4(a) shows the simulated electro-optic signal produced by a 10 MeV bunch with 1 ps duration traveling at $y_B = 1$ mm distance from the upper side of the crystal. As outlined by Fig. 2(b), the geometry of the EOS setup produces signals with curved shapes. In Fig. 4(b) the

Optics EXPRESS

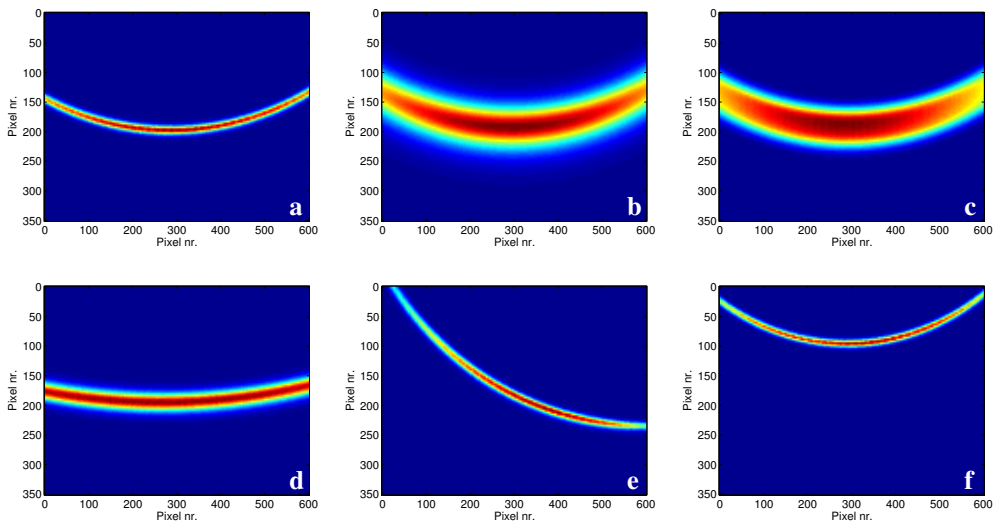

Fig. 4. Numerical simulations of the electro-optic signals produced by using the bunch parameters summarized in Table 1. The plots show the simulated output detected by the CCD camera. The charge is 1 nC in all cases.

mean beam energy is decreased to 1 MeV and, as a result, the resulting signal appears wider because of the field opening in the longitudinal direction ($\propto r/\gamma$). If compared to Fig. 4(c), corresponding to an higher energy bunch (10 MeV) with longer duration (10 ps), the signals are very similar. In order to distinguish between these possible situations, an independent measure of the mean energy or duration is needed. In our case we experimentally measured the mean energy by using the EOS as a time of flight monitor. This allows to discriminate such kind of signals. Another parameter affecting the signal shape is the distance between the traveling electrons and the observer (i.e. the ZnTe crystal in our case). Figure 4(d) shows the case in which the bunch vertical coordinate y_B is increased from 1 mm to 10 mm. The resulting signal is wider for the longitudinal field opening. Moreover it exhibits a less pronounced curvature due to the fact that the radial distance from the field source is increased. Figure 4(e) shows the effect of an horizontal offset $x_B = 3$ mm of the electron beam with respect to the crystal center. As a consequence the resulting signal is tilted toward the direction of the offset. This aspect is particularly useful in order to reconstruct the beam path after its emission from target. The last simulation, shown in Fig. 4(f), corresponds to a different delay ($\Delta t = 4$ ps) of the probe laser with respect to the same bunch of Fig. 4(a). The result consists in a signal shift toward the upper side of the crystal.

4. Experimental results

For the experimental measurements the distance between the ZnTe crystal and the path of the emitted electrons is set to $r \approx 1$ mm. Figure 5(a) reports a typical EOS snapshot, exhibiting the expected curved shape as outlined in Fig. 2(b). By delaying the arrival time of the probe laser onto the crystal, the position of the EOS signal changes accordingly. In this case we expect the signals to shift down, because in the meantime the induced local birefringence moved far from the path of the travelling electrons (cf. Figure 2(b)). This is shown in Fig. 5(c) and confirmed by the simulation in Fig. 5(f). By anticipating the probe laser the behavior is the opposite (cf. Fig. 5(b) and Fig. 5(e)). The mean velocity (and thus the energy) of the moving electrons is evaluated by measuring the delay of the EOS signal centroid with respect to the reference time. A good agreement with measurements is obtained by simulating an electron bunch with 2.1 nC

Optics EXPRESS

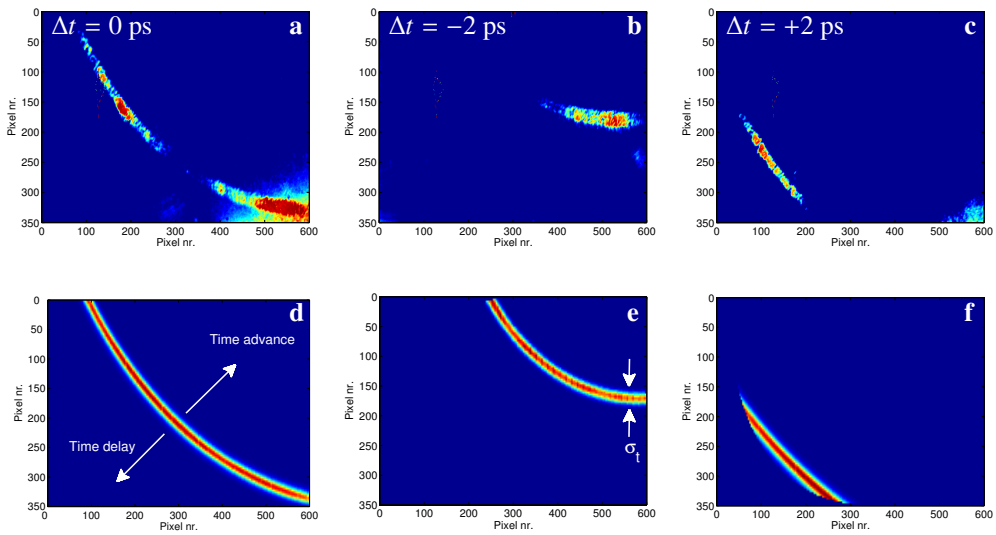

Fig. 5. (a-c) Experimentally measured EOS signals obtained by changing the probe laser delay (Δt) with respect to the main laser. For a delay (advance) of the probe laser, the resulting signals shift down (up). (d-f) Simulated EOS signals assuming the emitted electron cloud described in Sec. 4. The time direction is indicated by the white arrows in (d). The lack of uniformity in the experimental signals is mainly due to inhomogeneities both on the ZnTe crystal surface and on the transverse profile of the probe laser.

charge, 14 MeV energy and about 500 fs duration. The overall reproducibility of the experiment is proved by considering that the structure of the EOS signals in Fig. 5 (a-c) remains unaltered while the probe delay is changed shot-by-shot. This is confirmed by the numerical simulations in Fig. 5 (d-f). The lack of uniformity in the experimental signals, if compared with the simulated ones, is mainly due to inhomogeneities both on the ZnTe crystal surface and on the transverse profile of the probe laser.

According to the simulates EOS signals, once the mean energy of the traveling bunch is determined, the width of the signal itself is actually proportional to the bunch duration. Therefore the charge temporal profile can be obtained by performing a line-out along the time direction depicted in Fig. 5(a). The result, shown in Fig. 6, has been calculated by averaging a series of line-outs along the curved shape of the signal. The red line represents the simulated EOS signal profile of the snapshot shown in Fig. 5(d). Due to the spatial encoding setup, the time axis is retrieved by calibrating the CCD pixels as $\Delta t_{pixel} = (\Delta x_{pixel}/c) \cdot \sin\theta_i \approx 15$ fs, where Δx_{pixel} is the pixel physical size. This result represents the first measurement ever done with sub-picosecond resolution of the fast electron component released in laser-matter interactions. Such charge profile shows that the 2.1 nC fast electrons are 'bunched' in time with a peak current of about 2 kA.

5. Conclusions

We have presented direct and temporally-resolved measurement of the first electrons ejected from solid targets. Our snapshots captured their evolution with sub-picosecond resolution and provide, at the same time, an evaluation of the total emitted charge, mean energy and temporal profile. They indicate that approximately 2.1 nC of fast electrons escaped from target and traveled up to the EOS crystal. By analyzing at the corresponding temporal profile, these electrons appear to be grouped in time with approximately 500 fs duration. By measuring their time of flight and

Optics EXPRESS

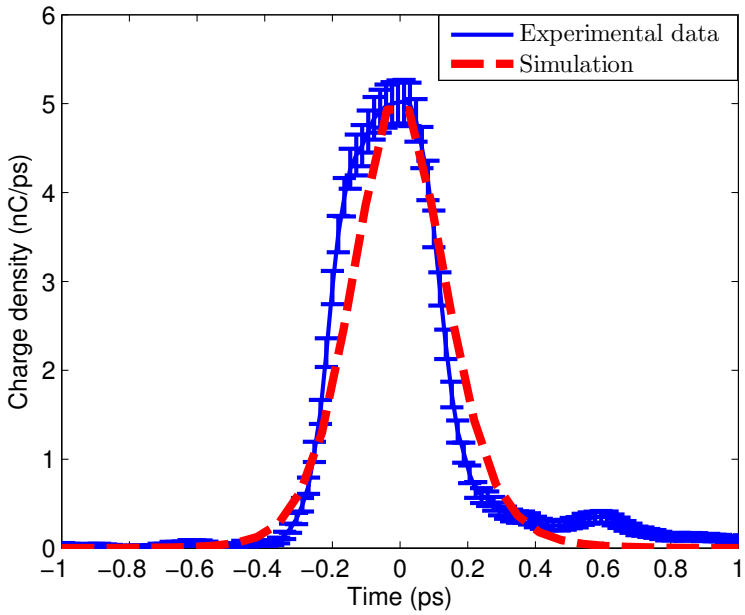

Fig. 6. Single-shot temporal profile of the snapshot reported in Fig. 5(a). The profile is obtained by averaging a series of line-outs performed along the time direction (white arrows). The errorbars are calculated as the standard deviation of such average. The red dashed line represents the corresponding profile provided by the numerical simulation of Fig. 5(d). The time axis is centered in correspondence of the signal peak.

comparing with simulations we obtain a mean energy of about 14 MeV. Since the measured fast electrons are responsible for the generation of the electrostatic potential, that in turn establishes the subsequent acceleration of protons and heavier ions, the EOS diagnostics represents a suitable tool in order to probe the temporal evolution of the induced potential barrier near the target surface and for a deeper understanding of the entire TNSA acceleration process.

Funding

EU Commission in the 7th Framework Program, Grant Agreement 312453-EuCARD-2. Italian Research Minister in the framework of FIRB - Fondo per gli Investimenti della Ricerca di Base, Project n. RBFR12NK5K. BSF foundation.